OPEN

Temperature-dependent photoluminescence in light-emitting diodes

Taiping Lu, Ziguang Ma, Chunhua Du, Yutao Fang, Haiyan Wu, Yang Jiang, Lu Wang, Longgui Dai, Haiqiang Jia, Wuming Liu & Hong Chen

Key Laboratory for Renewable Energy, Chinese Academy of Sciences; Beijing Key Laboratory for New Energy Materials and Devices, Beijing National Laboratory for Condensed Matter Physics, Institute of Physics, Chinese Academy of Sciences, Beijing 100190, China.

Temperature-dependent photoluminescence (TDPL), one of the most effective and powerful optical characterisation methods, is widely used to investigate carrier transport and localized states in semiconductor materials. Resonant excitation and non-resonant excitation are the two primary methods of researching this issue. In this study, the application ranges of the different excitation modes are confirmed by analysing the TDPL characteristics of GaN-based light-emitting diodes. For resonant excitation, the carriers are generated only in the quantum wells, and the TDPL features effectively reflect the intrinsic photoluminescence characteristics within the wells and offer certain advantages in characterising localized states and the quality of the wells. For non-resonant excitation, both the wells and barriers are excited, and the carriers that drift from the barriers can contribute to the luminescence under the driving force of the built-in field, which causes the existing equations to become inapplicable. Thus, non-resonant excitation is more suitable than resonant excitation for studying carrier transport dynamics and evaluating the internal quantum efficiency. The experimental technique described herein provides fundamental new insights into the selection of the most appropriate excitation mode for the experimental analysis of carrier transport and localized states in p-n junction devices.

ecause of its high accuracy and non-destructive nature, photoluminescence (PL) studies have been recognised as one of the most sensitive and widely employed methods of exploring the physical characteristics of materials, such as band structures[1–4], the luminescence of impurities[5,6], and point defects[7,8]. The PL technique is also a powerful and important tool for obtaining information regarding low-dimensional semiconductors, e.g., quantum-size effects[9–11], many-body processes[12,13], strain analysis[14–16], localized states[17–21], excitonic states[22,23], coupling effects[24,25], carrier relaxation processes and recombination mechanisms[26–31]. Because of the importance of luminescence phenomena, it is vitally important to be able to conduct a careful analysis of the process itself, including the generation, transport and recombination of carriers. Among these three processes, the transport of carriers plays a crucial role in linking the generation and recombination of carriers. Therefore, investigating the carrier transport mechanism in materials is of considerable importance.

Temperature-dependent photoluminescence (TDPL) is one of the most fundamental and technologically important tools for characterising semiconductor devices. Based on photoluminescence spectra measured at different temperatures, a systematic and mature theory has been developed to study the defects related to non-radiative processes[32,33], localized states[20,34], and carrier transport dynamics[20,35,36]. A series of physical equations are widely used to characterise and fit the above physical processes. In general, two different photon excitation energies are used to characterise the photoluminescence properties of quantum-well luminescence devices. The first is resonant excitation, in which the excitation energy is below the barrier band gap; hence, the carriers are generated only in wells[33,36]. The second approach is non-resonant excitation, in which the excitation energy is higher than the barrier band gap, and thus, both the barriers and the wells are excited[37–39]. In previous reports, for both resonant excitation and non-resonant excitation, the Arrhenius formula and the band-tail model have been widely used to describe carrier transport and localized states, respectively, in quantum-well structures[19–21,32,33,36,37,39]. However, these physical equations cannot accurately reflect the carrier transport and localized states for both excitation modes, and thus, they lead to an equivocal description of these physical processes.

1
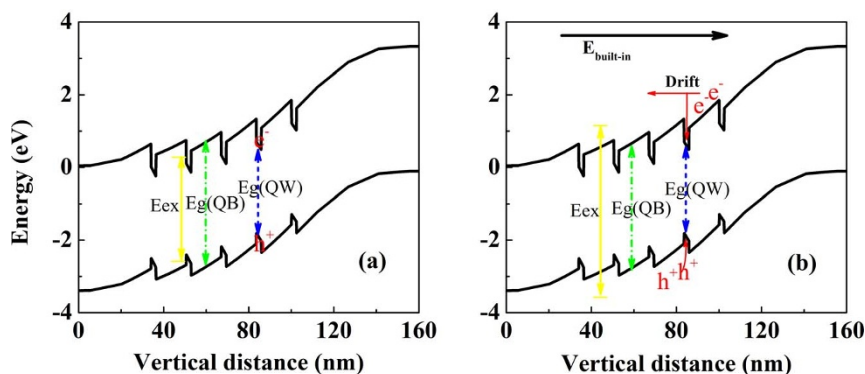
Figure 1 | Schematic diagrams of the PL process when the sample is excited. (a) When the excitation energy (Eex) is less than the band energy of the barrier (Eg(QB)), the wells are resonantly excited. Electrons and holes are generated only in the wells, and they will quickly relax from continuous states into quantum states to emit light. (b) Carriers are generated in both wells and barriers when non-resonant excitation is applied (Eex > Eg(QB)). Under the driving force of the built-in electric field, the electrons and holes will drift to opposite sides. During this process, the carriers may be captured by quantum states or non-radiative centres.

Hence, the physical origins of the different TDPL characteristics of the two excitation modes should be clarified, and the application ranges of the two excitation modes should be discussed.

In this work, InGaN multiple-quantum-well (MQW) light-emitting diodes (LEDs) are chosen as the particular subject of investigation to clarify the carrier transport and localization by applying different excitation modes. The trend of the variation in the TDPL characteristics measured using non-resonant excitation is significantly different from that measured using resonant excitation. The abnormal PL features observed under the non-resonant excitation mode cannot be well fitted using the commonly applied Arrhenius equation and band-tail mode. In previous reports, these abnormal PL characteristics have been attributed to carrier transport between the different localized states, but this explanation can be excluded based on the TDPL intensity measured under resonant excitation. We also propose that the different temperature-dependent PL characteristics are associated with carrier drift in the quantum barriers and that the driving force is the built-in electric field in the depletion region. Through comparison of the resonant and non-resonant TDPL results, the physical origins of the different optical features of the two modes are clarified, and the application ranges of the excitation modes can be defined.

Results

Photoluminescence mechanism. The MQW region is composed of five pairs of 2-nm-thick InGaN wells separated by 12-nm-thick, lightly Si-doped GaN (n-doping = 3×10^{17} cm^{-3}) barriers. The nominal indium content of the InGaN well is approximately 0.18.

In Fig. 1, the energy band structure of the InGaN/GaN-based LEDs is plotted to illustrate the PL mechanisms of the various excitation modes. Because of the large polarization field that exists in the MQW region, the energy band is sharply sloped[40–42]. For resonant excitation, the excitation energy is below the barrier gap, and thus, the carriers are generated only in the wells. The photogenerated carriers quickly relax from continuous states into quantum states, and electrons then radiatively recombine with holes to emit light. The quantum barriers (QBs) can prevent the carriers from moving in the growth direction of the material. Hence, the TDPL features under resonant excitation accurately reflect the intrinsic luminescence characteristics of the quantum wells. For non-resonant excitation, the excitation energy is higher than the barrier gap, and thus, both the barriers and the wells are excited. In this case, the measured TDPL characteristics should include information regarding both the carriers from the wells and the barriers. Because of the large built-in electric field, the photogenerated electrons and holes in the QBs will drift apart in the depletion region. During the drift process, the carriers may relax into QW states or be captured by the non-recombination centres.

The time-integrated PL spectra measured using a 325-nm laser and a 405-nm laser with fixed excitation powers of 30 mW and 1 mW, which were recorded between 10 K and 300 K, are presented in Fig. 2. It can be observed that the blue LED has a lower PL intensity under the resonant excitation condition at 10 K. However, the PL intensity excited by the 325-nm laser is greater than that excited by the 405-nm laser under an excitation power of 30 mW at 300 K, whereas this relation is reversed at 1 mW, as shown in Fig. 2(b).
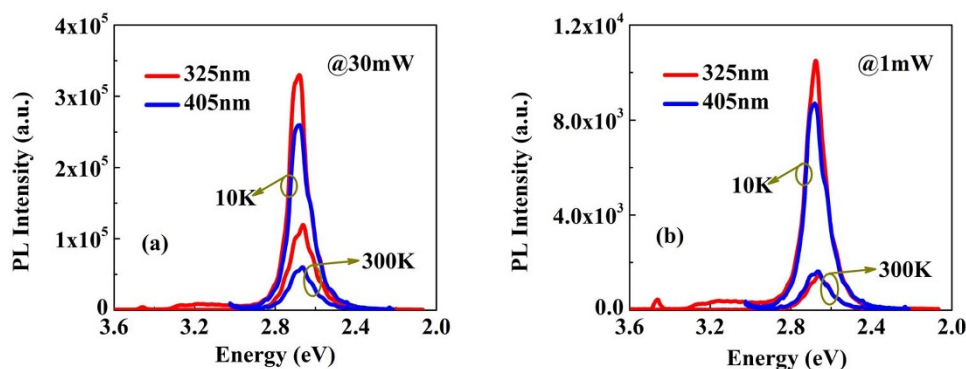
Figure 2 | The PL spectra measured under two excitation energies at temperatures of 10 K and 300 K. The blue LED has a lower PL intensity under the resonant excitation condition at 10 K. In Fig. 2(a), the PL intensity excited by the 325-nm laser is greater than that excited by the 405-nm laser under an excitation power of 30 mW at 300 K, whereas this relation is reversed at 1 mW, as shown in Fig. 2(b).
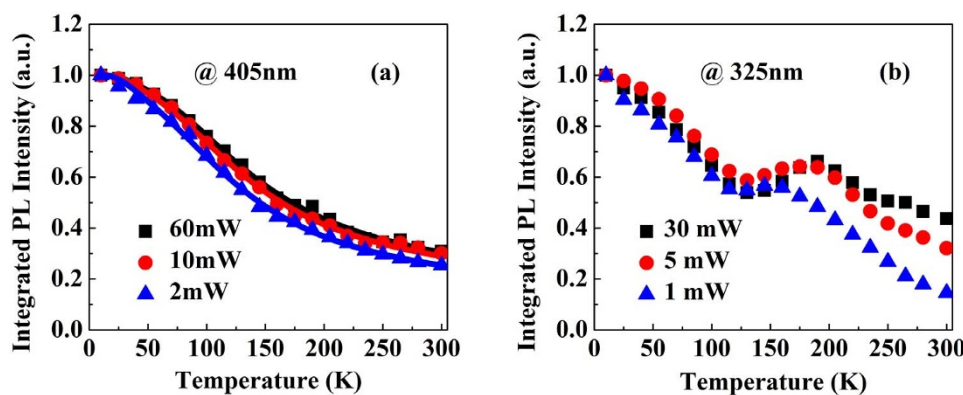
Figure 3 | Temperature-dependent integrated PL intensities of the LED structures under various excitation powers. (a) A monotonic decrease in the integrated PL intensity is generally observed when 405-nm excitation is applied. The solid curves represent the best fits for the PL quenching as a function of temperature, as obtained using the Arrhenius formula described in the text. (b) An anomalous temperature-dependent PL intensity is observed in the moderate temperature region (∼110–170 K) under excitation with a 325-nm laser.

The substantial variation in the ratio between the room-temperature PL intensities of the two excitation modes at different excitation powers can be attributed to the transport of carriers in the barriers, which will be discussed in a later section.

Temperature-dependent photoluminescence intensity. Typical temperature-dependent PL intensity (nearly exponential decay) curves of the LED samples under resonant excitation are presented in Fig. 3(a). The temperature-dependent PL intensity can be well fitted using the following Arrhenius formula[32,43–46]:

$$I(T) = \frac{1}{1 + C_1 \exp(\frac{-E_{A1}}{k_B T}) + C_2 \exp(\frac{-E_{A2}}{k_B T})}, \qquad (1)$$

where $I(T)$ represents the normalized integrated PL intensity. The parameters C_1 and C_2 are two constants related to the density of non-radiative recombination centres in the samples. E_{A1} and E_{A2} are the activation energies corresponding to the non-radiative recombination process[45–48]. k_B is Boltzmann's constant. All fitting results and the I_{300K}/I_{10K} ratios are listed in Table 1. Under the resonant excitation condition, the obtained fitting parameters exhibit high stability with respect to variations in the excitation power. The saturation of the non-radiative centres and the carrier-screening effect lead to smaller rate constants under high excitation. Nevertheless, the TDPL intensity of the non-resonant excitation cannot be fitted using the above equation, and the I_{300K}/I_{10K} ratio exhibits a strong dependence on the excitation power, as shown in Table 1. The trends of the variation in the PL intensities of the two excitation modes as the temperature increases from 10 K to 100 K are extremely similar. However, distinct temperature-dependent features manifest in the moderate-temperature region. A knee appears in the integrated PL intensity curves under non-resonant excitation, that is, the intensity gradually increases as the temperature increases. This anomalous phenomenon can be interpreted in terms of two possible explanations: the first is carrier transport along

the quantum barriers, and the second is carrier transport between different localized states[49,50]. This behaviour is not observed under resonant excitation. Hence, carrier transport between localized states cannot be the primary explanation for this phenomenon. The gradual increase in the PL intensity also makes it impossible to fit using the Arrhenius formula. There must exist one mechanism of carrier supplementation that can provide sufficient carriers to compensate for the temperature increase caused by the loss of carriers. Here, we propose that the observed anomalous optical phenomenon is associated with the carrier transport behaviour referred to as carrier mobility. Because of the competition between impurity scattering and lattice scattering, the carrier mobility increases with increasing temperature in the moderate-temperature region (∼80–200 K)[51,52]. The augmented carrier mobility will enhance the drift movement of the carriers under the driving force of the net electric field in the GaN barriers. Increasing the amount of carriers will serve to decrease the ratio between the densities of non-radiative recombination centres and radiative recombination centres, thus leading to a more efficient carrier-screening effect.

In GaN-based devices, holes have a very low mobility (∼5–10 cm²/V·s)[51,53], which makes it very difficult for holes to travel within the active region and be immediately captured by the nearby QW. By contrast, electrons have a relatively high mobility (∼200–500 cm²/V·s)[52,54]. Consequently, the electrons can easily travel in the opposite direction of the built-in field and ultimately be captured by the QWs. The accumulated carriers in the QWs are beneficial for diminishing the polarization field and increasing the radiative recombination efficiency[55,56]. Furthermore, the carrier-screening effect of ionized impurity (or defect) scattering can enhance the mobility of carriers[54,57]. Consequently, the PL intensity is elevated in the moderate-temperature region (∼120–170 K). In the high-temperature region (∼200–300 K), the activation of non-radiative recombination centres and the escape of carriers from the QWs lead to thermal quenching of the PL[46]. An alternative description of the trend of the variation in the TDPL intensity

Table 1 | The obtained fitting parameters: activation energies (E_{A1} and E_{A2}) and constants (C_1 and C_2) as well as the I_{300K}/I_{10K} ratio

Excitation energy	405 nm laser			325 nm laser		
Excitation power	2 mW	10 mW	60 mW	1 mW	5 mW	30 mW
C_1	0.79	0.56	0.45			
E_{A1} (meV)	8.46	8.79	8.63			
C_2	8.64	7.50	7.20			
E_{A2} (meV)	33.45	33.52	33.68			
I_{300K}/I_{10K}	25.4%	30.1%	30.9%	14.6%	32.1%	43.7%
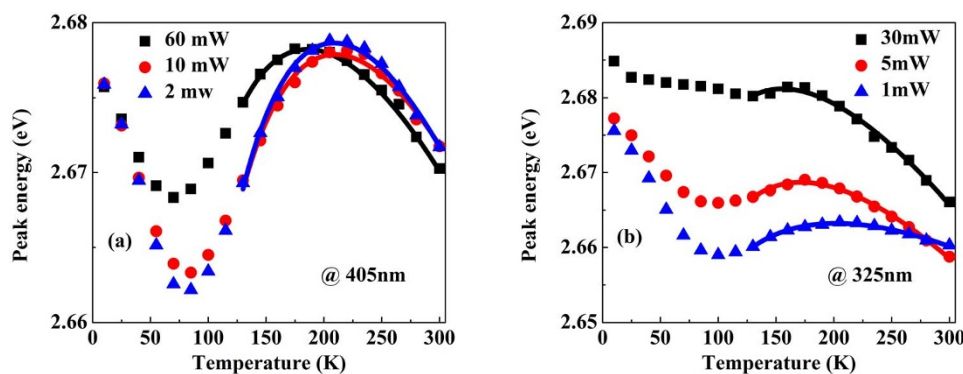
Figure 4 | Temperature-dependent Gauss-fitted peak energies of the LED structures under various excitation powers. The solid curves represent the best fits for the peak-energy shift as a function of temperature obtained using the band-tail model described in the text. (a) Under 405-nm excitation, an S-shaped shift in the peak energy related to the localized states is observed. The red-blue-red shift in the peak energy exhibits a minimal excitation-power dependence. (b) A strongly excitation-power-dependent shift in the peak energy is observed under excitation at 325 nm.

observed through time-resolved PL (TRPL) measurements can be expressed as follows[19,58]:

$$\eta_{int}(T) = \frac{\tau_{PL}(T)}{\tau_{rad}(T)} = \frac{1}{1 + \frac{\tau_{rad}(T)}{\tau_{nr}(T)}}, \quad (2)$$

where τ_{PL} is the carrier lifetime obtained from the TRPL measurement and τ_{rad} and τ_{nr} are the radiative and non-radiative carrier lifetimes, respectively. $\eta_{int}(T)$ is assumed to be equal to $I_{PL}(T)/I_{PL}(0\ K)$, with the assumption that $I_{PL}(0\ K) = 1$. Under resonant excitation, the thermally activated non-radiative centres and increased radiative lifetime lead to a decrease in the PL intensity. Under non-resonant excitation, a portion of the transported carriers are consumed by non-radiative centres; therefore, the remaining carriers can be captured by the radiative centres and enhance the PL intensity in the moderate-temperature region ($\sim$120–170 K). The greater enhancement of the PL intensity under high excitation can serve to decrease the ratio of the density of non-radiative recombination centres to the density of radiative recombination centres. Consequently, the non-radiative lifetime of the carriers can be expressed as follows[59]:

$$\tau_{nr} = \frac{1}{N_{nr}\sigma V_{th}}, \quad (3)$$

where N_{nr} is the density of non-radiative centres. σ and v_{th} represent the carrier capture cross section of non-radiative centres and the carrier velocity, respectively. Because of the differences in defect density, carrier capture cross section and carrier velocity, the non-radiative lifetimes of the two excitation modes are different. Combing the carrier drift behaviour under non-resonant excitation, the differences in the TDPL intensity can be effectively explained.

The internal quantum efficiency (IQE) is one of the most important parameters of an LED, and it can be defined as the ratio of the number of photons generated to the number of injected electrons and holes, which is often expressed as the ratio of the integrated PL intensity between 300 K and 0 K[60–62]. However, in practice, it is very difficult to reach 0 K, and the PL intensity at 0 K can only be obtained by extrapolating the trend of the variation in the PL intensity in the low-temperature region (<20 K). When the QWs are under resonant excitation, the carriers are generated only in QWs and no carriers transport along the QBs. Hence, the value of the IQE obtained by measuring the PL intensity ratio may not accurate. Under the non-resonant excitation condition, the photogenerated carriers in the QBs will drift in the active region and be captured by the recombination and non-recombination centres. This situation is analogous to carrier injection under a low current density: the

injected holes and electrons will travel through the active region under the driving force of the built-in field. Most importantly, the relation between the photo-excitation power and the IQE obtained under non-resonant optical pumping is very similar to that of the electrical pumping in the low-current region. In other words, the IQE will gradually increase because of the carrier-filling effect of the non-radiative centres at a high pumping density. The highly similar variation trends of the IQE under different pumping methods can be attributed to the carrier drift in the active region induced by the built-in electric field. The minimal change in the I_{300K}/I_{10K} with varying excitation power under resonant excitation also supports the above explanation. Hence, non-resonant excitation is advantageous for investigating carrier transport in the active region and characterising the nominal IQE.

Temperature-dependent photoluminescence spectral characteristics. Figure 4(a) shows the Gauss-fitted TDPL peak energies at various excitation powers under resonant excitation. The large S-shaped shift behaviour of the peak energy is characteristic of the localization effect. The degree of the localization effect can be determined by fitting the temperature-dependent emission energy curve using the band-tail model[63–65]:

$$E(T) = E_g(0) - \frac{\alpha T^2}{T + \beta} - \frac{\sigma^2}{k_B T}, \quad (4)$$

where $E(T)$ is the emission energy at T, $E_g(0)$ is the energy gap at 0 K, and α and β are the Varshni coefficients. The third term originates from the localization effect, and σ indicates the degree of the localization effect, where in general, a larger value of σ corresponds to a stronger localization effect. k_B is the Boltzmann constant. The obtained fitting parameters are presented in Table 2. The initial red-blue shift of the peak energy can be explained in terms of carrier transport between shallow and deep localization centres. In the high-temperature region, the narrowing of the band gap with increasing temperature leads to a red shift of the peak energy. In general, the localization effect will be reduced under high-excitation conditions because of the carrier delocalization effect[20], which is consistent with the localized energies obtained under resonant excitation, as shown in Table 2. However, an abnormal relation between the localized effect and the excitation power is observed under the non-resonant excitation condition. As the excitation power decreases from 30 mW to 1 mW, the value of σ initially exhibits a slight increase and then dramatically decreases. Because the mobility of the carriers and the activation of the non-recombination centres are closely related to the temperature, the number of drift carriers captured by the QWs should be dependent on temperature, and this dependence is

Table 2 | The obtained fitting parameters: carrier location energies (σ) under different excitation conditions

Excitation energy	405 nm laser			325 nm laser		
Excitation power	2 mW	10 mW	60 mW	1 mW	5 mW	30 mW
σ (meV)	24.70	23.58	18.70	14.82	17.56	17.21

responsible for the anomalous trend of the variation in the localization effect.

Figure 5 presents the Gauss-fitted TDPL full widths at half maximum (FWHMs) under various excitation powers. A U-shaped FWHM related to localized states is generally observed for both resonant and non-resonant excitation conditions. The redistribution of carriers in the shallow and deep localized states leads to a narrowing of the emission line width in the low-temperature region, followed by a monotonic broadening with increasing temperature up to room temperature. The primary difference between the two excitation modes is in the moderate-temperature region (80–170 K). The FWHM value decreases as the temperature increases under resonant excitation. By contrast, under non-resonant excitation, the enhanced carrier drift movement results in the non-uniform redistribution of the carriers, followed by a slight broadening of the line width. The similar broadening of the FWHM in the high-temperature region (200–300 K) is caused by coupling of the excitons to acoustic phonons and to LO phonons[66].

Discussion

It should be noted that the observed distinct TDPL features are closely associated with carrier transport in the active region over the entire temperature region (10–300 K), especially in the moderate-temperature region (~100–170 K). Because of the competition between different scattering mechanisms, strongly temperature-dependent carrier mobility causes the number of drift carriers captured by the QWs to vary with temperature. Consequently, abnormal TDPL spectral characteristics are observed under non-resonant excitation. By contrast, the TDPL characteristics measured under resonant excitation can be well explained using the Arrhenius equation and the band-tail mode. The excitation-power-dependent rate constants and localized energies directly reflect the non-recombination centres and localized states in the QWs. These results indicate that resonant excitation offers certain advantages when analysing the localized states within the QWs and evaluating the quality of the quantum wells, whereas it cannot accurately characterise the carrier transport in the active region or the IQE. Instead, non-resonant excitation is superior for investigating carrier transport and characterising the nominal IQE. Nevertheless, non-resonant excita-

tion cannot reveal the intrinsic photoluminescence features of the QWs. Finally, the equivocal physical processes of carrier transport and localization have been clarified.

It is very important to understand the role played by the quantum barriers in this work. In low-dimensional quantum structures, the wide-gap barrier can serve as a wall that confines the carriers in narrow-gap materials. When the excitation energy is less than the energy gap of the barrier, the carriers are generated only in the potential wells and the barriers can prevent the carriers from moving into adjacent wells. With no external field applied to the device, the TDPL characteristics can be well explained using the Arrhenius equation and the band-tail mode. When non-resonant excitation is applied, the photogenerated carriers in the barriers will drift apart under the driving force of the electric field. The carriers will be captured by both radiative and non-radiative recombination centres during the drift process. In this scenario, the measured TDPL characteristics reflect the combined effect of the photogenerated carriers in the wells and the captured drift carriers from the barriers, which causes the currently used physical equations to no longer be applicable; thus, a new physical model should be developed to analyse the carrier transport process in low-dimensional semiconductor structures.

In this work, the application ranges of the excitation modes are defined. In p-n junction devices, a built-in field always exists, even when no external field is applied. Under non-resonant excitation, the carriers will drift apart under the driving force of the built-in field, which commonly exists in many other optoelectronic devices, such as photodiodes and solar cells. Hence, the results obtained in this work will play a guiding role in the analysis of such physical processes, and the experimental technique described herein can be applied to investigate optical features of p-n junction devices.

Methods

Epitaxial growth of LED structures. The InGaN-based blue LED structures were grown on c-sapphire substrates using metal-organic chemical vapour deposition (MOCVD). The precursors were trimethylgallium (TMGa), triethylgallium (TEGa), trimethylindium (TMIn), and ammonia (NH$_3$). Silane (SiH$_4$) and bis-cyclopentadienyl magnesium (Cp$_2$Mg) were used as n-type and p-type dopants, respectively. Before the deposition of a GaN nucleation layer, the sapphire wafer was thermally cleaned at 1170°C under an H$_2$ atmosphere for 10 min. A 25-nm-thick GaN nucleation layer was grown at 530°C and annealed at 1050°C under an NH$_3$
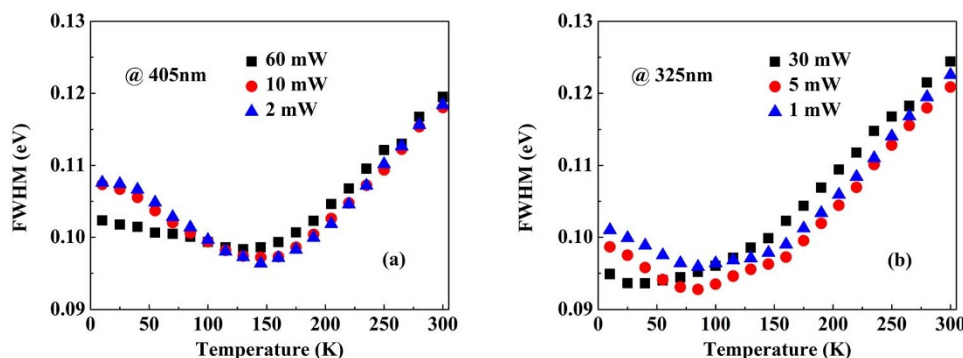
Figure 5 | Temperature-dependent Gauss-fitted full widths at half maximum (FWHMs) of the LED structures under various excitation powers.
(a) A U-shaped FWHM shift related to carrier redistribution in different localized states in the low-temperature region and phonon broadening in the high-temperature region are observed under excitation at 405 nm. (b) Two FWHM-broadening slopes are observed in the moderate-to-high-temperature region when a 325-nm laser is applied. In the moderate-temperature region, the FWHM broadening is associated with carrier drift.

flow, followed by a 500-nm-thick, nominally undoped GaN layer and a 3.5-μm-thick, Si-doped GaN (n-doping = 5×10^{18} cm^{-3}) layer at a temperature of 1100°C under a reactor pressure of 400 mbar. In the following steps, five pairs of InGaN/GaN MQWs with 2-nm-thick InGaN wells separated by 12-nm-thick, lightly Si-doped GaN (n-doping = 3×10^{17} cm^{-3}) barriers were grown under a nitrogen atmosphere. The growth temperatures of the InGaN wells and GaN barriers were 730 and 830°C, respectively. A 10-nm-thick, undoped GaN spacer layer was grown after the QWs, and a 200-nm-thick, Mg-doped GaN (p-doping = 8×10^{17} cm^{-3}) was then deposited as a p-type contact layer at 930°C.

X-ray analysis. High-resolution X-ray diffraction (HRXRD) was performed using a Bede D1 double-axis diffractometer with a parabolic graded multiplayer Gutman mirror collimator followed by a four-bounce channel-cut Si (2 2 0) monochromator, delivering a Cu K$_{\alpha 1}$ line with a wavelength of λ = 0.154056 nm. The indium content and the thicknesses of the quantum well and barrier as measured via HRXRD were 17.78% and 2.03 and 11.92 nm, respectively.

Photoluminescence measurements. The temperature dependence of the luminescence spectra was determined by cooling each sample in a closed-loop He cryostat to ~8 K and then gradually heating to 300 K. A 325-nm He-Cd continuous wave laser and a 405-nm laser diode were selected as the excitation sources. The optical path was held constant to ensure identical test conditions. The size of the light spot focused on the samples was approximately 0.1 mm. The output power could be adjusted from 30 mW to 0.3 mW using a neutral optical attenuator. The luminescence was dispersed by a triple-grating 50-cm monochromator and detected by a GaAs photomultiplier tube using the conventional lock-in technique.

1. Ithurria, S. et al. Colloidal nanoplatelets with two-dimensional electronic structure. Nature Mater. 10, 936–941 (2011).
2. Glaser, E. et al. Detection of magnetic resonance on photoluminescence from a Si/Si$_{1-x}$Ge$_x$ strained-layer superlattice. Phys. Rev. Lett. 65, 1247–1250 (1990).
3. Whittaker, D. M., Fisher, T. A., Simmonds, P. E., Skolnick, M. S. & Smith, R. S. Magneticfield-induced indirect gap in a modulation-doped quantum well. Phys. Rev. Lett. 67, 887–890 (1991).
4. Arsenault, A. C. et al. From colour fingerprinting to the control of photoluminescence in elastic photonic crystals. Nature Mater. 5, 179–184 (2006).
5. Gaul, D. A. & Rees, W. S. True blue inorganic optoelectronic devices. Adv. Mater. 12, 935–946 (2000).
6. Monemar, B. et al. Evidence for two Mg related acceptors in GaN. Phys. Rev. Lett. 102, 235501 (2009).
7. Kan, D. et al. Blue-light emission at room temperature from Ar$^+$-irradiated SrTiO$_3$. Nature Mater. 4, 816–819 (2005).
8. Godefroo, S. et al. Classification and control of the origin of photoluminescence from Si nanocrystals. Nature Nanotech. 3, 174–178 (2008).
9. Cullis, A. G. & Canham, L. T. Visible light emission due to quantum size effects in highly porous crystalline silicon. Nature 353, 335–338 (1991).
10. Lu, Z. H., Lockwood, D. J. & Baribeau, J.-M. Quantum confinement and light emission in SiO$_2$/Si superlattices. Nature 378, 258–260 (1995).
11. de Boer, W. D. A. M. et al. Red spectral shift and enhanced quantum efficiency in phonon-free photoluminescence from silicon nanocrystals. Nature Nanotech. 5, 878–884 (2010).
12. Latta, C. et al. Quantum quench of Kondo correlations in optical absorption. Nature 474, 627–630 (2011).
13. Skolnick, M. S. et al. Observation of a many-mody edge singularity in quantum-well luminescence spectra. Phys. Rev. Lett. 58, 2130–2133 (2009).
14. Sess, M. J. et al. Analysis of enhanced light emission from highly strained germanium microbridges. Nature Photon. 7, 467–472 (2013).
15. Gershoni, D. et al. Optical transitions in quantum wires with strain-induced lateral confinement. Phys. Rev. Lett. 65, 1631–1634 (1990).
16. De Sousa Pereira, S. M., O'Donnell, K. P. & Da Costa Alves, E. J. Role of nanoscale strain inhomogeneity on the light emission from InGaN epilayers. Adv. Funct. Mater. 17, 37–42 (2007).
17. Kaneta, A., Funato, M. & Kawakami, Y. Nanoscopic recombination processes in InGaN/GaN quantum wells emitting violet, blue and green spectra. Phys. Rev. B. 78, 125317 (2008).
18. Bardoux, R. et al. Positive binding energy of a biexciton confined in a localization center formed in a single In$_x$Ga$_{1-x}$N/GaN quantum disk. Phys. Rev. B. 79, 155307 (2008).
19. Chichibu, S. F. et al. Origin of defect-insensitive emission probability in In-containing (Al,In,Ga)N alloy semiconductors. Nature Mater. 5, 810–816 (2006).
20. Schomig, H. et al. Probing individual localization centers in an InGaN/GaN quantum well. Phys. Rev. Lett. 92, 106802 (2004).
21. De, S. et al. Two distinct origins of highly localized luminescent centers within InGaN/GaN quantum-well light-emitting diodes. Adv. Funct. Mater. 21, 3828–3835 (2011).
22. Snoke, D., Denev, S., Liu, Y., Pfeiffer, L. & West, K. Long-range transport in excitonic dark states in coupled quantum wells. Nature 418, 754–757 (2002).
23. Szczytko, J. et al. Determination of the exciton formation in quantum wells from timeresolved interband luminescence. Phys. Rev. Lett. 93, 137401 (2004).
24. Gibbs, H. M., Khitrova, G. & Koch, S. W. Exciton-polariton light-semiconductor coupling effects. Nature Photon. 5, 275–282 (2011).
25. Reithmaier, J. P. et al. Strong coupling in a single quantum dot-semiconductor microcavity system. Nature 432, 197–200 (2004).
26. Toda, Y., Moriwaki, O., Nishioka, M., Arakawa, Y. & Arakawa, Y. Efficient carrier relaxation mechanism in InGaAs/GaAs self-assembled quantum dots based on the existence of continuum states. Phys. Rev. Lett. 82, 4114–4117 (1999).
27. Wang, X. et al. Non-blinking semiconductor nanocrystals. Nature 459, 686–689 (2009).
28. Sturm, J. C. et al. Well-resolved band-edge photoluminescence of excitons confined in strained Si$_{1-x}$Ge$_x$ quantum wells. Phys. Rev. Lett. 66, 1362–1365 (1991).
29. Lobo, C. et al. Inhibited carrier transfer in ensembles of isolated quantum dots. Phys. Rev. B. 60, 16647–16651 (1999).
30. Pinos, A., Marcinkevicius, S. & Shur, M. S. Inhibited carrier transfer in ensembles of isolated quantum dots. J. Appl. Phys. 109, 103108 (2011).
31. Siegert, J., Marcinkevicius, S. & Zhao, Q. X. Carrier dynamics in modulation-doped InAs/GaAs quantum dots. Phys. Rev. B. 72, 085136 (2005).
32. Ryu, S. W. et al. Analysis of improved efficiency of InGaN light-emitting diode with bottom photonic crystal fabricated by anodized aluminum oxide. Adv. Funct. Mater. 19, 1650–1655 (2009).
33. Okamoto, K. et al. Surface-plasmon-enhanced light emitters based on InGaN quantum wells. Nature Mater. 3, 601–605 (2004).
34. Szendrei, K. et al. Exploring the origin of the temperature-dependent behavior of PbS nanocrystal thin films and solar cells. Adv. Funct. Mater. 22, 1598–1605 (2012).
35. Yamada, Y., Yasuda, H., Tayagaki, T. & Kanemitsu, Y. Temperature dependence of photoluminescence spectra of nondoped and electron-doped SrTiO$_3$: crossover from Auger recombination to single-carrier trapping. Phys. Rev. Lett. 102, 247401 (2009).
36. Ko, Y. H. et al. Electrically driven quantum dot/wire/well hybrid light-emitting diodes. Adv. Mater. 23, 5364–5369 (2011).
37. Choi, J. H. et al. Nearly single-crystalline GaN light-emitting diodes on amorphous glass substrates. Nature Photon. 5, 763–769 (2011).
38. Oto, T., Banal, R. G., Kataoka, K., Funato, M. & Kawakami, Y. 100 mW deep-ultraviolet emission from aluminium-nitride-based quantum wells pumped by an electron beam. Nature Photon. 4, 767–771 (2010).
39. Kwon, M. K. et al. Surface-plasmon-enhanced light-emitting diodes. Adv. Mater. 20, 1253–1257 (2008).
40. Lu, T. et al. Advantages of GaN based light-emitting diodes with a p-InGaN hole reservoir layer. Appl. Phys. Lett. 100, 141106 (2012).
41. Lu, T. et al. Effect of Stair-Case Electron Blocking Layer on the Performance of Blue InGaN Based LEDs. J. Disp. Technol. 10, 146–150 (2014).
42. Lu, T. et al. Improvement of light power and efficiency droop in GaN-based LEDs using graded InGaN hole reservoir layer. Appl. Phys. A. 114, 1055–1059 (2014).
43. Bimberg, D., Sondergeld, M. & Grobe, E. Thermal Dissociation of Excitons Bounds to Neutral Acceptors in High-purity GaAs. Phys. Rev. B. 4, 3451–3455 (1971).
44. Hao, M., Zhang, J., Zhang, X. H. & Chua, S. Photoluminescence studies on InGaN/GaN multiple quantum wells with different degree of localization. Appl. Phys. Lett. 81, 5129–5131 (2002).
45. Deng, Z. et al. A novel wavelength-adjusting method in InGaN-based light-emitting diodes. Sci. Rep. 3, 3389 (2013).
46. Zheng, X. H. et al. Influence of the deposition time of barrier layers on optical and structural properties of high-efficiency green-light-emitting InGaN/GaN multiple quantum wells. J. Appl. Phys. 96, 1899–1903 (2004).
47. Hwang, J. S. et al. Direct comparison of optical characteristics of InGaN-based laser diode structures grown on pendeo epitaxial GaN and sapphire substrates. Appl. Phys. Lett. 90, 131908 (2007).
48. Liu, L. et al. Influence of indium composition in the prestrained InGaN interlayer on the strain relaxation of InGaN/GaN multiple quantum wells in laser diode structures. J. Appl. Phys. 109, 073106 (2011).
49. Polimeni, A., Patan, A., Henini, M., Eaves, L. & Main, P. C. Temperature dependence of the optical properties of InAs/Al$_y$Ga$_{1-y}$As self-organized quantum dots. Phys. Rev. B. 59, 5064–5068 (1999).
50. Ma, J. et al. Anomalous temperature dependence of photoluminescence in self-assembled InGaN quantum dots. Appl. Phys. Lett. 101, 131101 (2012).
51. Simon, J., Protasenko, V., Lian, C., Xing, H. & Jena, D. Polarization-induced hole doping in wide-band-gap uniaxial semiconductor heterostructures. Science 327, 60–64 (2010).
52. Wang, T. et al. Effect of silicon doping on the optical and transport properties of InGaN/GaN multiple-quantum-well structures. Appl. Phys. Lett. 76, 1737–1739 (2000).
53. Kaufmann, U., Schlotter, P., Obloh, H., Köhler, K. & Maier, M. Hole conductivity and compensation in epitaxial GaN:Mg layers. Phys. Rev. B. 62, 10867–10872 (2000).
54. Ng, H. M., Doppalapudi, D., Moustakas, T. D., Weimann, N. G. & Eastman, L. F. The role of dislocation scattering in n-type GaN films. Appl. Phys. Lett. 73, 821–823 (1998).
55. Kim, T.-S. et al. Well-to-well non-uniformity in InGaN/GaN multiple quantum wells characterized by capacitance-voltage measurement with additional laser illumination. Appl. Phys. Lett. 100, 071917 (2012).
56. Waltereit, P. et al. Nitride semiconductors free of electrostatic fields for efficient white lightemitting diodes. Nature 406, 865–858 (2000).

57. Rode, D. L. & Gaskill, D. K. Electron Hall mobility of n-GaN. *Appl. Phys. Lett.* **66**, 1972–1973 (1995).

58. Kaneta, A. *et al.* Discrimination of local radiative and nonradiative recombination processes in an InGaN/GaN single-quantum-well structure by a time-resolved multimode scanning near-field optical microscopy. *Appl. Phys. Lett.* **83**, 3462–3464 (2003).

59. Gelhausen, O. *et al.* Dissociation of H-related defect complexes in Mg-doped GaN. *Phys. Rev. B.* **69**, 125210 (2004).

60. Pimputkar, S., Speck, J. S., Denbaars, S. P. & Nakamura, S. Prospects for LED lighting. *Nature Photon.* **3**, 180–182 (2009).

61. Armstrong, A. M., Crawford, M. H. & Koleske, D. D. Contribution of deep-level defects to decreasing radiative efficiency of InGaN/GaN quantum wells with increasing emission wavelength. *Appl. Phys. Exp.* **7**, 032101 (2014).

62. Seetoh, I. P. *et al.* Improvement in the internal quantum efficiency of InN grown over nanoporous GaN by the reduction of Shockley-Read-Hall recombination centers. *Appl. Phys. Lett.* **103**, 121903 (2013).

63. Eliseev, P. G., Perlin, P., Lee, J. & Osinski, M. "Blue" temperature-induced shift and band-tail emission in InGaN-based light sources. *Appl. Phys. Lett.* **71**, 569–571 (1997).

64. Kaneta, A. *et al.* Nanoscopic Photoluminescence Properties of a Green-Emitting InGaN Single Quantum Well on a {20$\bar{2}$1} GaN Substrate Probed by Scanning Near-Field Optical Microscopy. *Appl. Phys. Exp.* **5**, 102104 (2012).

65. Funato, M. *et al.* Remarkably Suppressed Luminescence Inhomogeneity in a (0001) InGaN Green Laser Structure. *Appl. Phys. Exp.* **6**, 111002 (2013).

66. Franssen, G., Litwin-Staszewska, E., Piotrzkowski, R., Suski, T. & Perlin, P. Optical and electrical properties of homoepitaxially grown multiquantum well InGaN/GaN light-emitting diodes. *J. Appl. Phys.* **94**, 6122–6128 (2003).

Acknowledgments

Author contributions

T.L., H.C. and Z.M. conceived the study. T.L. and C.D. conducted the sample-growth experiments. T.L. and Y.F. performed the variable-temperature photoluminescence measurements. H.C. supervised the entire research project. T.L., H.C., Z.M., H.W., Y.J., L.W., L.D., H.J. and W.L. analysed the data. All authors discussed the results and wrote the manuscript.

Additional information

Competing financial interests: The authors declare no competing financial interests.

How to cite this article: Lu, T. *et al.* Temperature-dependent photoluminescence in light-emitting diodes. *Sci. Rep.* **4**, 6131; DOI:10.1038/srep06131 (2014).